Electronic Supplementary Information

Ultrasmall Sn nanoparticles embedded in spherical hollow carbon for enhanced lithium storage properties

Ning Zhang,*[ab] Yuanyuan Wang,[a] Ming Jia,[a] Yongchang Liu,*[bc] Jianzhong Xu,*[a] Lifang Jiao[b] and Fangyi Cheng[b]

[a] *College of Chemistry & Environmental Science, Key Laboratory of Analytical Science and Technology of Hebei Province, Hebei University, Baoding 071002, China. E-mail: ningzhang@hbu.edu.cn, xujz@hbu.edu.cn*

[b] *Key Laboratory of Advanced Energy Materials Chemistry (Ministry of Education), College of Chemistry, Nankai University, Tianjin 300071, China.*

[c] *Institute for Advanced Materials and Technology, University of Science and Technology Beijing, Beijing 100083, China. E-mail: liuyc@ustb.edu.cn*

Experimental Section

Material Synthesis: Hollow-structured Sn@HC composite with ~5 nm Sn nanoparticles uniformly embedded in the shell of hollw spherical carbon matrix was synthesized by an one-pot and template-free aerosol spray pyrolysis method, as schematically illustrated in Figure 1. In the typical synthesis, dissolving 3.9 g resorcinol in 5.0 mL formaldehyde at room temperature, and then evaporating the extra water in the mixture at 50 ^{o}C for 2 h to prepare the resorcinol formaldehyde (RF) resin colloidal solution. The as-prepared RF resin and 0.05 M $SnCl_2$ were dissolved in 250 mL ethanol–water mixed solvent with 10 vol.% water, and then the mixture was stirred to obtain a clear solution. The precursor solution was atomized with an argon flow using a constant-output nebulizer under the gauge pressure of 0.2 MPa. Subsequently, aerosol droplets were passed through a tubular furnace at 800 ^{o}C for a residence time of ~2 s. In this case, the surface precipitation of Sn salt and RF components occurs due to the faster evaporation rate of enthanol than water, resulting in hollow structured spheres. It is noted that the solubility of Sn salt and RF resin in ethanol is much higher than that of the counterparts in water. The thermal pyrolysis of $SnCl_2$ and the carbonization RF resin could simultaneously take place, thus generating the Sn@HC composite. The collected final product was centrifuged and washed thoroughly with ethanol solvent, and then dried at 80 ^{o}C for 10 h in vacuum. Because metal ions act as catalysts to promote the formation of carbon in a short time, the hollow carbon spheres cannot be produced directly if the precursor solution does not contain Sn salts. For comparison, the Sn@SC composite with solid structure can be synthesized using similar procedures with that of Sn@HC, besides the concentration of $SnCl_2$ changed to 0.2 M. This result is mainly due to that the surface enrichment effect will be much weakened as incresing the heavy/concentration of precursor sulution. In addition, the Sn-C hollow composite with lower Sn mass loading was prepared by just decreasing the $SnCl_2$ concentration to 0.02 M in percursor solution. Moreover, the Sn-C solid composite was fabricated using similar procedures with that of Sn@HC, but employing ethanol as solvent without adding water. The pyrolyzed cabon was synthesized by the thermal decomposition of RF resin colloidal solution at 700 ^{o}C for 1 h in Ar atmosphere. The pure Sn powder was purchased from Sigma-Aldrich.

Materials Characterization: Powder XRD patterns were collected on a Rigaku X-ray diffractometer (MiniFlex600) with Cu Kα radiation. The 2θ angular region from 10^o to 80^o was performed at a scan rate of 4^o min^{-1}. SEM images were taken on Field-emission JEOL JSM7500F microscope. TEM and HRTEM images were obtained on Philips Tecnai G2 F20. Raman spectra were tested on confocal Thermo-Fisher Scientific DXR microscope using 532 nm excitation. XPS spectra were recorded on PerkinElmer PHI 1600 ESCA. TGA was measured by a Netzsch STA 449 F3 Jupiter analyzer with a heating rate 5 ^{o}C min^{-1} in air from room temperature to 600 ^{o}C. After TGA experiment, the carbon and Sn component in the composite were oxidized into CO_2 (gas) and SnO_2 (solid), respectively. The Sn content can be calculated based on the following Equation S1:

$$\text{Sn (wt\%)} = \frac{\text{molecular weight Sn}}{\text{molecular weight } SnO_2} \times \frac{\text{final weight}}{\text{initial weight}} \times 100 \quad \text{(S1)}$$

Electrochemical Measurements: Electrochemical performance was evaluated using CR2032 coin-type cells assembled in an argon-filled glove box with water and oxygen contents below 5 ppm. The working electrodes were fabricated by blending the active material, Super P carbon, and sodium carboxymethyl cellulose (CMC) in a weight ratio of 8:1:1 using water as solvent. The obtained slurry was pasted onto copper foil and then dried at 100 ^{o}C for 10 h in vacuum. The loading mass of active material was 1.5–2.0 mg cm^{-2}. Glass fiber and lithium metal were employed as separator and counter/reference electrode, respectively. The electrolyte was 1.0 M $LiPF_6$ in ethylene carbonate/dimethyl carbonate (EC/DMC, in 1:1 volume ratio) solution. The assembled cells were galvanostatically cycled in the voltage range of 0.05–2.0 V at different rates, using LAND-CT2001A battery-testing instrument. The applied current densities and the obtained capacities are based on the total mass of Sn@C composites. CVs were conducted on a LK2010A electrochemical workstation at various scan rates. EIS was performed on a Parstat 2273 electrochemical workstation (AMETEK). The AC perturbation signal was ± 10 mV and the frequency ranged from 100 kHz to 100 mHz. Before EIS test, the cells were first discharged/charged at 0.5 A g^{-1} for 5 cycles to stabilize the cell.

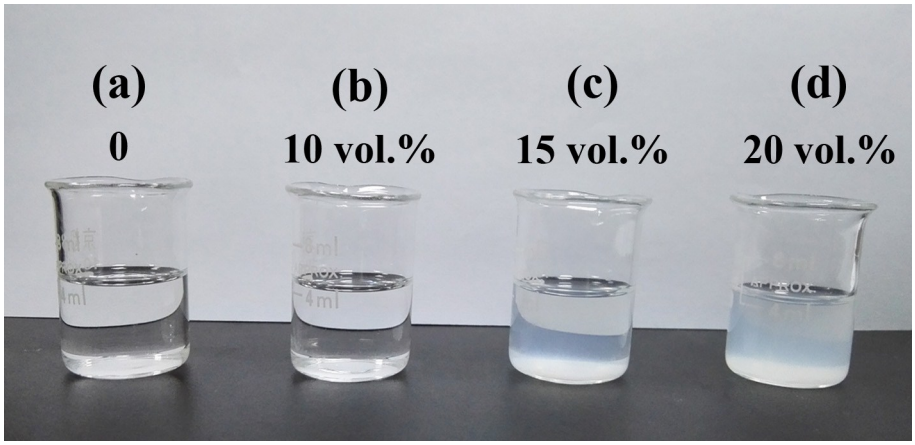

Figure S1. Digital photos of the precursor solutions with 0, 10, 15, and 20 vol.% water, respectively. The pH values at 20 °C of (b), (c), and (d) are 2.61, 2.46, and 2.34, respectively, measured by a pH meter (INSEA, PHS-3C). With the water content increasing to 15 vol.%, the clear solution turns into suspension due to the hydrolysis of $SnCl_2$ ($SnCl_2 + H_2O = Sn(OH)Cl \downarrow + HCl$).

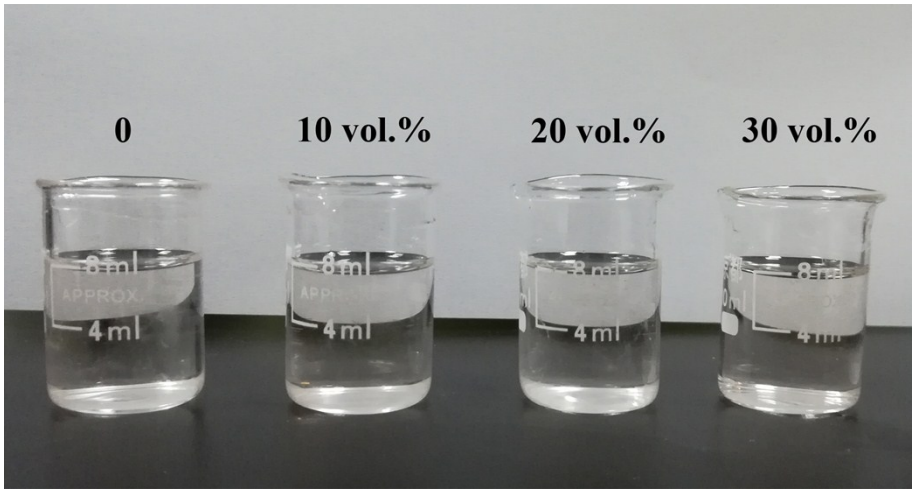

Figure S2. Digital photos of the RF resin-ethanol mixed solutions (without $SnCl_2$) with 0, 10, 20, and 30 vol.% water, respectively. The as-prepared RF resin can be very easily dissolved in ethanol. No obvious suspension can be found, even when the water content increases up to 30 vol.%.

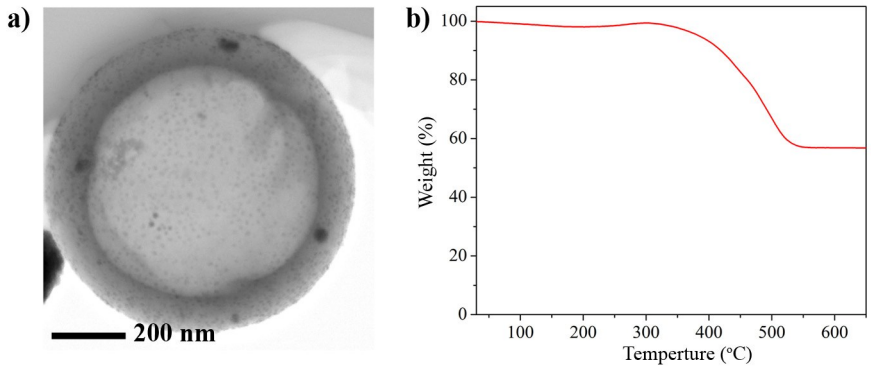

Figure S3. (a) Scanning transmission electron microscopy (STEM) image and (b) Thermogravimetric (TG) curve of the Sn-C hollow composite prepared using the low concentration solution with 0.02 M $SnCl_2$. It can be seen that fewer Sn nanoparticles are randomly embedded in a hollow carbon microsphere, compared with Sn@HC as shown in Fig. 1c. Based on the TG data, the active Sn mass loading is 42% in this composite.

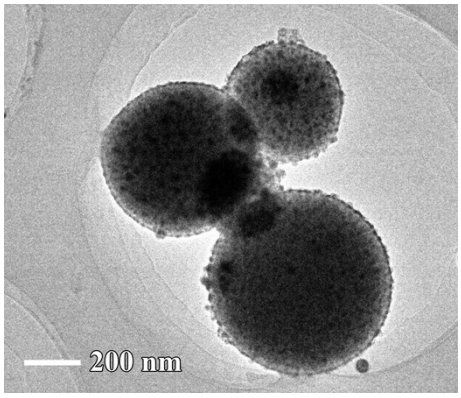

Figure S4. TEM image of the Sn-C solid composite prepared employing ethanol solvent without adding water.

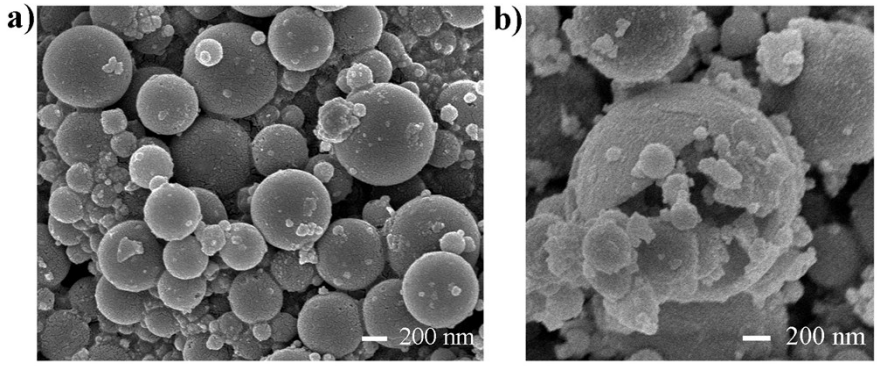

Figure S5. (a) Low-magnification SEM image of the as-prepared Sn@HC composite. (b) SEM image of a caved Sn@HC sphere.

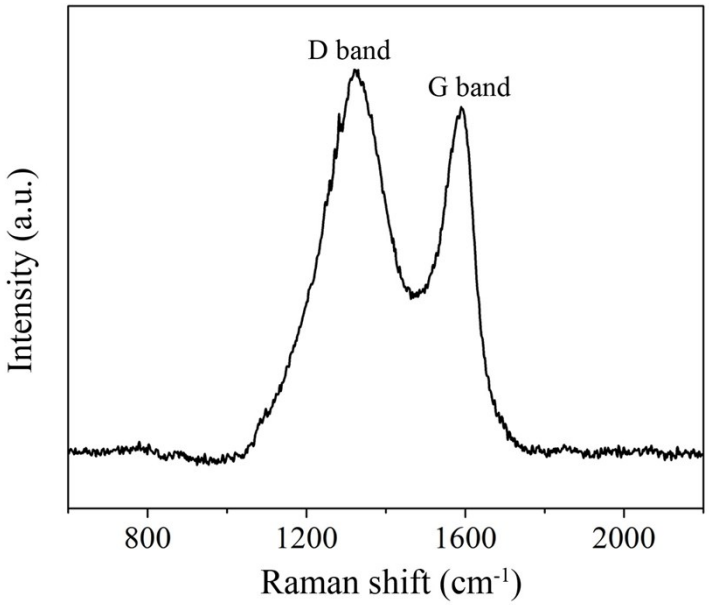

Figure S6. Raman spectrum of the as-prepared Sn@HC composite.

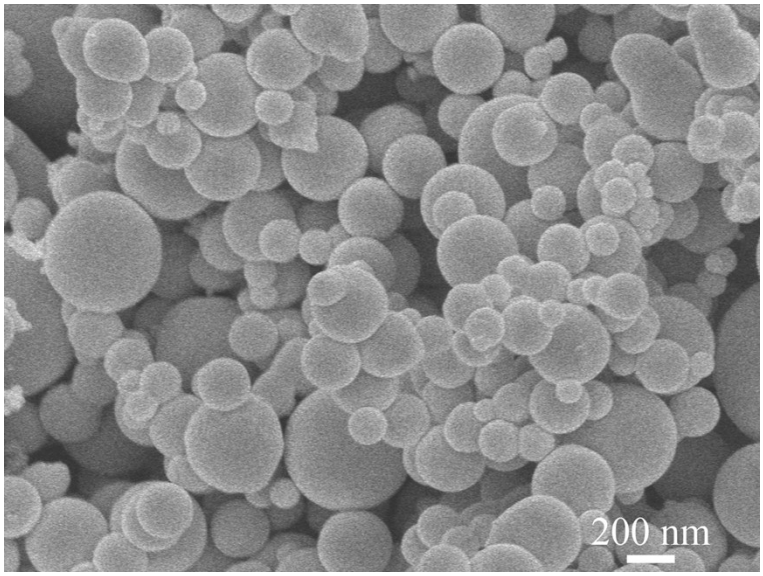

Figure S7. SEM image of commercial Sn particles.

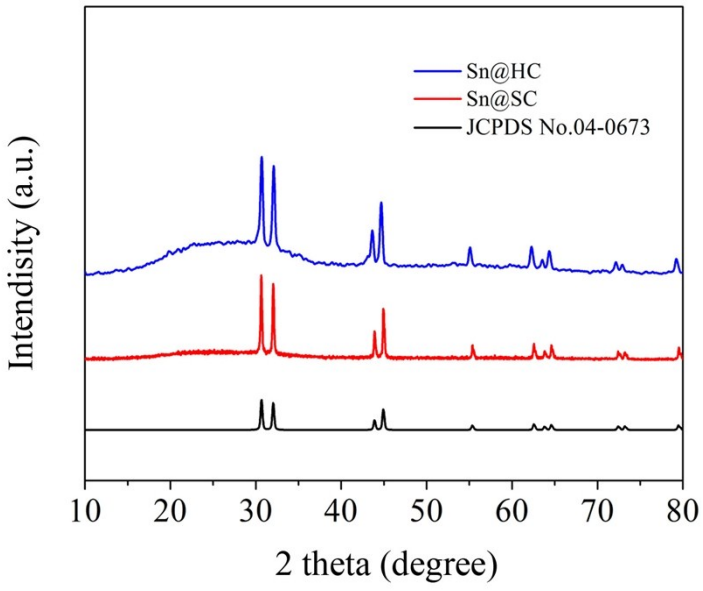

Figure S8. XRD patterns of Sn@HC and Sn@SC composites in comparison with standard card (JCPDS no. 04-0673).

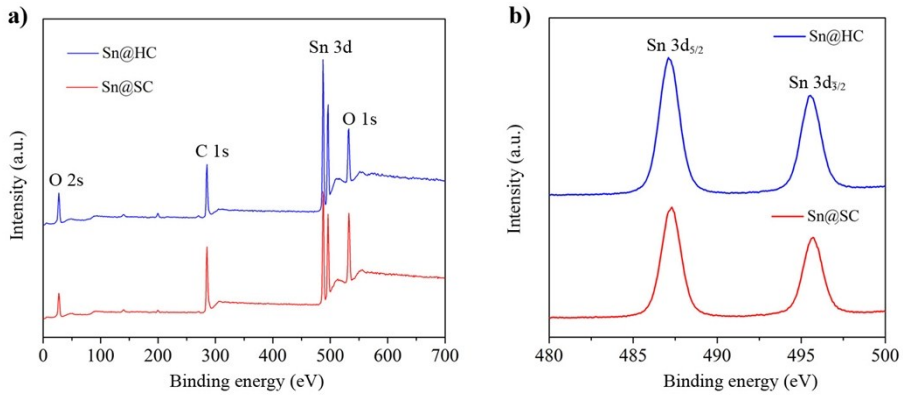

Figure S9. (a) XPS survey scans and (b) Sn 3d XPS spectra of Sn@HC and Sn@SC composites. The Sn 3d spectra show two characteristic peaks at 487.3 eV (Sn $3d_{5/2}$) and 495.7 eV (Sn $3d_{3/2}$), indicating that some Sn nanoparticles near the surface of the carbon matrix have been partially oxidized into SnO_2.[4,5]

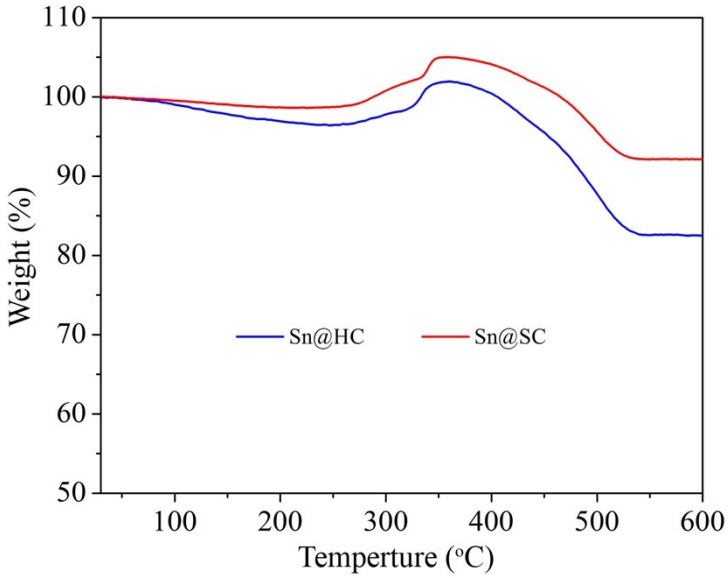

Figure S10. Thermogravimetric curves of Sn@HC and Sn@SC composites in air from 30 to 600 °C at a heating rate of 5 °C min^{-1}. In the temperature range of 30 to 200 °C, almost no weight loss was observed, indicating that the composite was stable in air up to 200 °C. From 200 °C to 350 °C, the weight increase was due to the oxidation of metallic tin ($Sn + O_2 = SnO_2$). The subsequent weight loss in the range of 350 °C to 520 °C was attributed to the combustion of carbon component ($C + O_2 = CO_2$).

Pseudocapacitive contribution calculation: The ratio of pseudocapacitive contribution can be quantitatively determined by separating the current response i at a fixed potential (V) into capacitive effect (k_1v) and diffusion-controlled insertion ($k_2v^{1/2}$) according to the Equation S2[1-3]:

$$i = k_1v + k_2v^{1/2} \quad \text{(S2)}$$

where i is the peak current, and v is sweep rate.

For analytical purpose, we rearrange Equation S2 slightly to Equation S3:

$$iv^{-1/2} = k_1v^{1/2} + k_2 \quad \text{(S3)}$$

The k_1 and k_2 values can be calculated based on Equation S3, by reading the peak currents (i) at the same potential from different sweep rates (v). For example, at the potential of 0.5 V during anodic process, we read five response currents ($i_{0.1}$, $i_{0.2}$, $i_{0.4}$, $i_{0.8}$ and $i_{1.6}$) at the corresponding sweep rates (0.1, 0.2, 0.4, 0.8 and 1.6 mV s^{-1}). Then, we plotted the linear behavior of sweep rates vs. currents, as shown in Figure S11. According to Equation S3, the k_1 value can be determined from the slope of the fitted line. Using this procedure, we are able to obtain other k_1 values at different potentials (V). Thus, the capacitive contribution was depicted in Fig. 2b (shaded region) by plotting the capacitance-dominated current (k_1v) vs. potential (V). Finally, the ratio of capacitance contribution can be determined by comparing the shaded area with the total stored charge. This calculated method refers to previous reports (B. Dunn, et al. *Nat. Mater.*, 2010, **9**, 146; B. Dunn, et al. *J. Phys. Chem. C* 2007, 111, 14925).

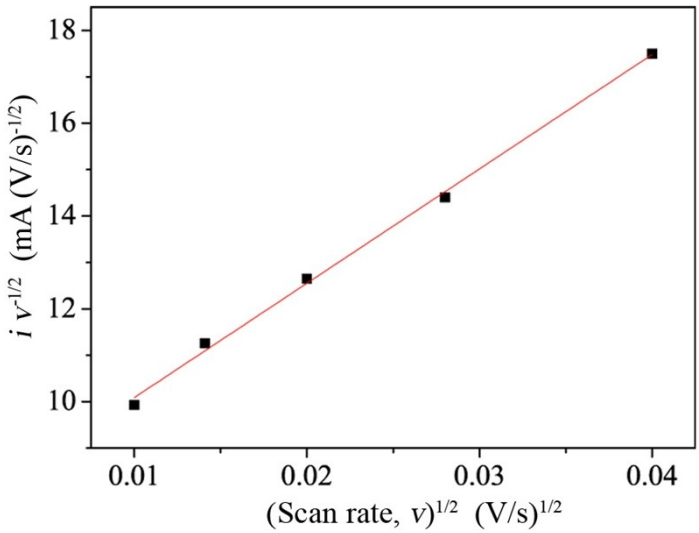

Figure S11. The linear relationship between sweep rates and response currents at 0.5 V during anodic process, according to Equation S3. Sweep rates are 1, 2, 4, 8 and 16 $\times 10^{-4}$ V s^{-1}, respectively.

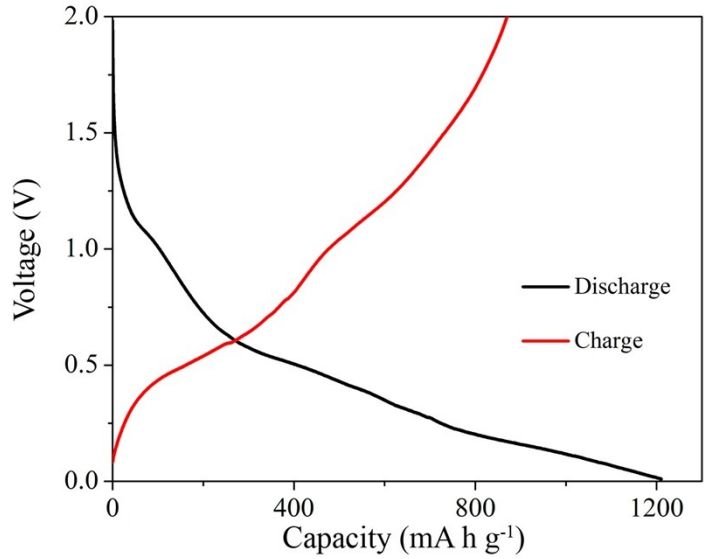

Figure S12. The initial discharge/charge profiles of the Sn@HC electrode at 0.5 A g^{-1}.

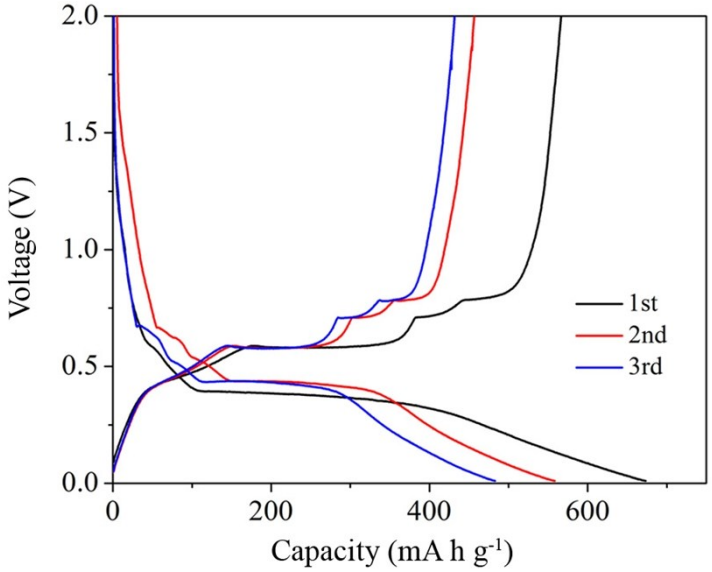

Figure S13. Discharge/charge profiles at 0.2 A g^{-1} for the pure commercial Sn electrode.

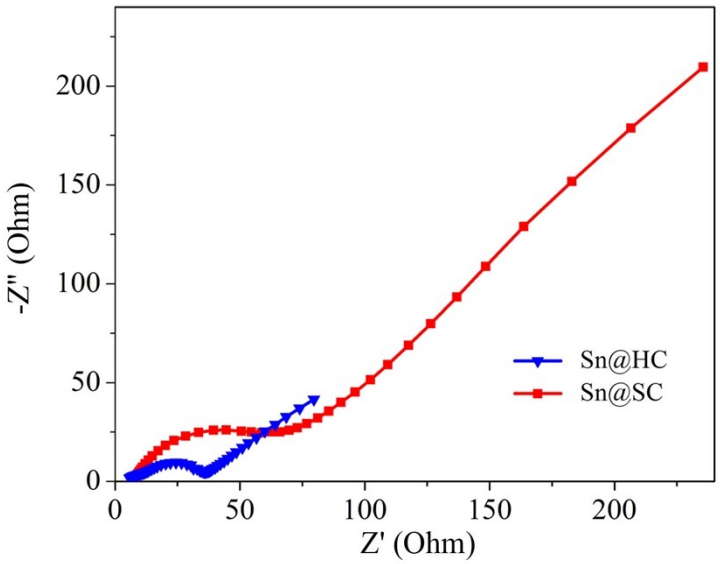

Figure S14. Electrochemical impedance spectra of Sn@HC and Sn@SC electrodes, collected at 0.5 V after five cycles.

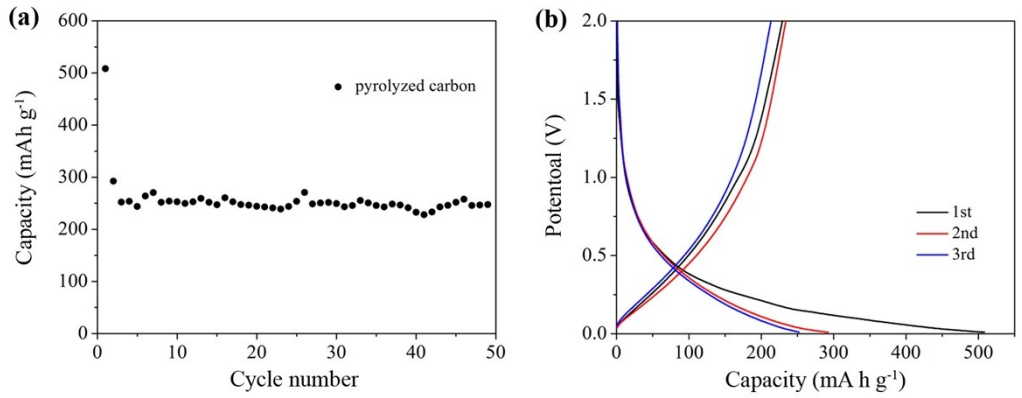

Figure S15. (a) Cycling performance and (b) discharge/charge profiles at 0.2 A g^{-1} for the pyrolyzed carbon electrode.

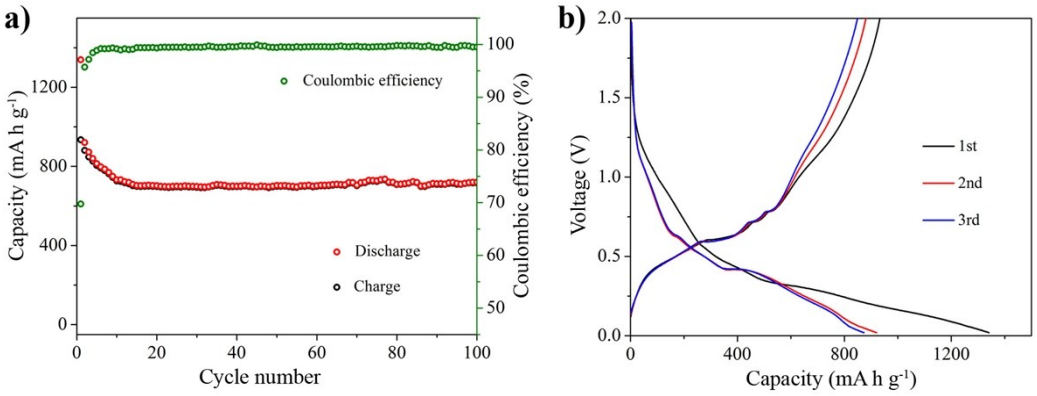

Figure S16. (a) Cycling performance and (b) discharge/charge profiles at the initial three cycles of the Sn@HC electrode at a low current density of 0.15 A g^{-1}.

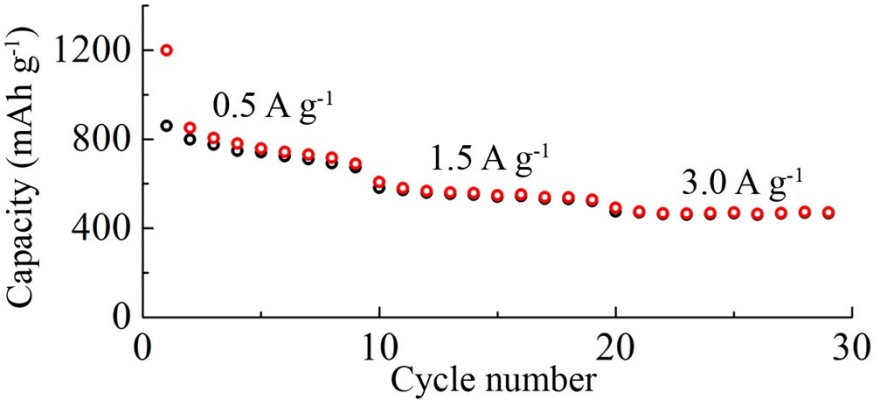

Figure S17. The capacity evolution at the initial 29 cycles of the Sn@HC anode.

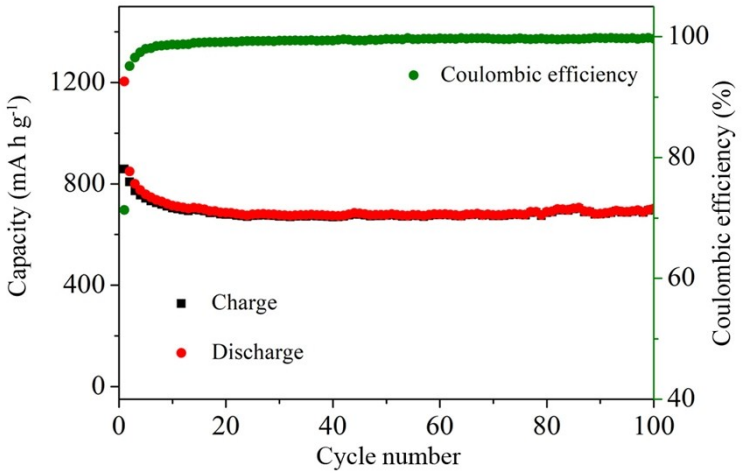

Figure S18. Cycling performance of the Sn@HC electrode at 0.5 A g^{-1}.

Table S1. Comparison of the as-prepared Sn@HC composite with previously reported Sn anodes for LIBs.

Samples	Synthetic procedure	Sn size and Sn content	Electrochemical performance	Ref.
Sn encapsulated in elastic hollow carbon spheres	Multiple steps using SiO_2 as template	60-100 nm, 75 wt%	550 mAh g^{-1} at 0.167 A g^{-1} after 100 cycles	6
Sn encapsulated in spherical hollow carbon	Multiple steps using RF sol as template	50-200 nm, 24 wt%	~300 mAh g^{-1} at 0.05 A g^{-1} after 10 cycles	7
Sn@carbon nanoparticles encapsulated in bamboo-like hollow carbon nanofibers	Electrospinning technique with multiple steps	~100 nm, 66 wt%	650 mAh g^{-1} at 0.5 A g^{-1}, 480 mAh g^{-1} at 2.5 A g^{-1}	8
Sn nanoparticles encapsulated in CNTs	Multiple steps using MnO_x as template	~70 nm, 67.3 wt%	749 mAh g^{-1} at 0.2 A g^{-1} with 71% capacity retention after 100 cycles, 602 mAh g^{-1} at 2 A g^{-1}, 377 mAh g^{-1} at 5 A g^{-1}	9
Yolk–shell Sn@C nanoboxes	Multiple steps using *in-situ* formed Zn as template	~100 nm, 70 wt%	720 mAh g^{-1} at 0.5 A g^{-1}, 430 mAh g^{-1} at 2 A g^{-1}, 350 mAh g^{-1} at 4 A g^{-1}	10
Sn/N-doped carbon microcage composite	Spray drying process followed by thermal treatment	5-10 nm, 51.8 wt%	472 mAh g^{-1} at 0.2 A g^{-1} after 500 cycles with 60 % capacity rentention	11
Sn-C nanocomposite	Sol-gel method	36 nm, 50 wt%	450 mAh g^{-1} after 100 cycles at 0.1 A g^{-1}	12
Sn nanoparticles embedded in N-doped porous carbon network	One-pot process by carbonizing Sn(Salen)	5 nm, 58 wt%	700 mAh g^{-1} at 0.5 A g^{-1}, 610 mAh g^{-1} at 1 A g^{-1}, 480 mAh g^{-1} at 5 A g^{-1}	13
Nano-Sn@C composite	Aerosol based method	10 nm, 62 wt%	600 mAh g^{-1} at 0.75 A g^{-1}, 550 mAh g^{-1} at 1.51 A g^{-1}, 550 mAh g^{-1} at 1.51 A g^{-1}, 390 mAh g^{-1} at 3.78 A g^{-1}, 260 mAh g^{-1} at 7.56 A g^{-1}	14

RGO-supported tin-core/carbon-sheath nanocables	Chemical vapor deposition (CVD) method	~100 nm in diameter and several micrometers in length, 61 wt%	630 mAh g^{-1} at 0.1 A g^{-1} after 50 cycles, 550 mAh g^{-1} at 0.4 A g^{-1} 350 mAh g^{-1} at 1.6 A g^{-1}	15
Graphene/Sn-nanopillar multilayered nanocomposite	Self-assembly and conventional film processing approaches	150–200 nm, 70 wt%	508 mAh g^{-1} at 0.5 A g^{-1} after 40 cycles, 408 mAh g^{-1} at 5 A g^{-1}	16
Core/shell Sn–C–Ni composite thin film	Electron beam evaporation	0.5–2 μm, 93 wt%	600 mAh g^{-1} at 0.27 A cm^{-2} g^{-1} after 40 cycles	17
Sn particles encapsulated in porous multichannel carbon microtubes	Single-nozzle electrospinning technique	200 nm, 66 wt%	295 mAh g^{-1} at 2 A g^{-1} after 50 cycles	18
Sn@HC	One-pot and template-free method using a modified aerosol spray pyrolysis technology	5 nm, 68.1 wt%	743 mAh g^{-1} at 0.5 A g^{-1}, 607 mAh g^{-1} at 1 A g^{-1}, 450 mAh g^{-1} at 4 A g^{-1}, 383 mAh g^{-1} at 8 A g^{-1}, 423 mAh g^{-1} over 6000 repeated cycles with 92.1% capacity retention even at 4 A g^{-1}	This work

Supplementary References

1. T. Brezesinski, J. Wang, S. H. Tolbert and B. Dunn, *Nat. Mater.*, 2010, **9**, 146.

2. J, Wang, J. Polleux, J. Lim, and B. Dunn, *J. Phys. Chem. C* 2007, **111**, 14925.

3. Z. Hu, Z. Z. Qiang, F. Y. Cheng, K. Zhang, J. B. Wang, C. C. Cheng and J. Chen, *Energy Environ. Sci.* 2015, **8**, 1309.

4. Z. Zhu, S. Wang, J. Du, Q. Jin, T. Zhang, F. Cheng and J. Chen, *Nano Lett.*, 2014, **14**, 153.

5. X. Han, Y. Liu, Z. Jia, Y.-C. Chen, J. Wan, N. Weadock, K. J. Gaskell, T. Li and L. Hu, *Nano Lett.*, 2013, **14**, 139.

6. W.-M. Zhang, J.-S. Hu, Y.-G. Guo, S.-F. Zheng, L.-S. Zhong, W.-G. Song and L.-J. Wan, *Adv. Mater.*, **2008**, *20*, 1160.

7. K. T. Lee, Y. S. Jung and S. M. Oh, *J. Am. Chem. Soc.*, 2003, **125**, 5652.

8. Y. Yu, L. Gu, C. Wang, A. Dhanabalan, P. A. van Aken and J. Maier, *Angew. Chem. Int. Ed.*, 2009, **48**, 6485.

9. X. Zhou, L. Yu, X.-Y. Yu and X. W. Lou, *Adv. Energy Mater.*, 2016, **6**, 1601177.

10. H. Zhang, X. Huang, O. Noonan, L. Zhou and C. Yu, *Adv. Funct. Mater.*, 2017, **27**, 1606023.

11. H. Ying, S. Zhang, Z. Meng, Z. Sun and W.-Q. Han, *J. Mater. Chem. A*, 2017, **5**, 8334

12. J. Hassoun, G. Derrien, S. Panero and B. Scrosati, *Adv. Mater.*, 2008, **20**, 3169.

13. Z. Zhu, S. Wang, J. Du, Q. Jin, T. Zhang, F. Cheng and J. Chen, *Nano Lett.*, 2014, **14**, 153.

14. Y. H. Xu, Q. Liu, Y. J. Zhu, Y. H. Liu, A. Langrock, M. R. Zachariah and C. S. Wang, *Nano Lett.*, 2013, **13**, 470.

15. B. Luo, B. Wang, M. Liang, J. Ning, X. Li and L. Zhi, *Adv. Mater.*, 2012, **24**, 1405.

16. L. Ji, Z. Tan, T. Kuykendall, E. J. An, Y. Fu, V. Battaglia and Y. G. Zhang, *Energy Environ. Sci.*, 2011, **4**, 3611.

17. R. Hu, H. Liu, M. Zeng, H. Wang and M. Zhu, *J. Mater. Chem.*, 2011, **21**, 4629.

18. Y. Yu, L. Gu, C. Zhu, P. A. van Aken and J. Maier, *J. Am. Chem. Soc.*, 2009, **131**, 15984.